J. Fluid Mech. (2004), *vol.* 517, *pp.* 1–25.
DOI: 10.1017/S0022112004000448 Printed in the United Kingdom

Vorticity interaction mechanisms in variable-viscosity heterogeneous miscible displacements with and without density contrast

By A. RIAZ AND E. MEIBURG†

Department of Mechanical and Environmental Engineering, University of California, Santa Barbara, CA 93106

(Received 9 June 2003 and in revised form 30 April 2004)

The vorticity interaction mechanisms governing miscible displacements in three-dimensional heterogeneous porous media are investigated by means of detailed simulations in the regimes of viscous fingering, dispersion, and resonant amplification. The computational results for spatially periodic and random permeability distributions are analysed in detail with respect to the characteristic wavenumbers and norms associated with the individual vorticity components. This allows the identification of the mechanisms dominating specific parameter regimes. Nominally axisymmetric displacements such as the present quarter five-spot configuration are particularly interesting in this respect, since some of the characteristic length scales grow in time as the front expands radially. This leads to displacement flows that can undergo resonant amplification during certain phases, while being dominated by fingering or dispersion at other times. The computational results also provide insight into the effects of density-driven gravity override on the interactions among these length scales. While this effect is known to play a dominant role in homogeneous flows, it is suppressed to some extent in heterogeneous displacements, even for relatively small values of the heterogeneity variance. This is a result of the coupling between the viscous and permeability vorticity fields in the viscous fingering and resonant amplification regimes. In the dispersive regime, gravity override is somewhat more effective because the coupling between the viscous and permeability vorticity fields is less pronounced, so that the large-scale structures become more responsive to buoyancy effects.

1. Introduction

The central issue in the analysis of displacements through heterogeneous porous media concerns the interaction between the permeability variation and the intrinsic instability mechanism related to an adverse mobility gradient. Several earlier investigations (e.g. Christie & Bond 1987; Araktingi & Orr 1988; Moissis, Miller & Wheeler 1989; Waggoner, Castillo & Lake 1992; Tchelepi & Orr 1993, 1994; Tchelepi 1994; Zhang, Sorbie & Tsibuklis 1997) demonstrate that either viscous fingering or permeability-induced channelling can dominate the displacement process, depending on the viscosity ratio, as well as the variance and correlation length of the permeability field.

† Author to whom correspondence should be addressed.

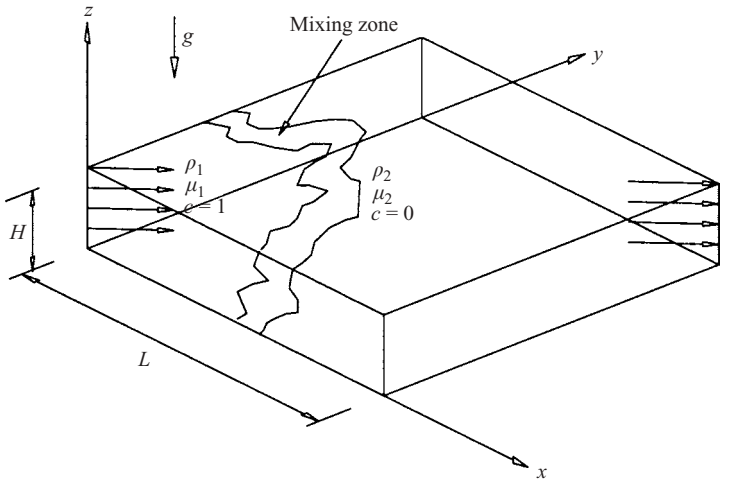

FIGURE 1. The three-dimensional computational domain.

De Wit & Homsy (1997*a*) investigate the problem at a more fundamental level, by means of a linear stability analysis of a rectilinear displacement in the presence of periodic permeability variations. They show that the growth of the viscous instability is amplified due to a harmonic resonance that occurs when the transverse wavenumbers of the permeability variation and the viscous instability are in an integral multiple relationship. A sideband resonance can occur if the sum of these wavenumbers is equal to the most amplified wavenumber of the homogeneous case. For streamwise permeability variations, the authors demonstrate that an amplification of the growth can occur when the inverse frequency at which the front encounters permeability oscillations is equal to the intrinsic dispersive time. Tan & Homsy (1992) briefly examine nonlinear aspects of miscible displacements through a random permeability field for rectilinear flows. By means of numerical simulations, they confirm the existence of a resonance mechanism for the random heterogeneity case as well. Camhi, Ruith & Meiburg (2000) use a vorticity based approach to study the coupling between the viscous and permeability related vorticity components in two-dimensional rectilinear flows, both for neutrally buoyant and variable-density displacements. They point out that the coupling between the viscous and permeability vorticity fields leads to a retardation of the gravity layer.

The present investigation addresses three-dimensional miscible displacements in doubly periodic arrangements of injection and production wells such as the well-known quarter five-spot configuration, cf. figure 1. This configuration, while being of practical importance, has several features that add to the complexity of the displacement. Near the injection source, the flow field is nominally axisymmetric, whereas later it becomes more nearly rectilinear. In their recent linear stability analysis of helical perturbations in radially evolving flows, Riaz & Meiburg (2003*a*) show that such flows are more sensitive to three-dimensional effects than unidirectional flows. This behaviour carries over to the nonlinear regime of homogeneous flows as well (Riaz & Meiburg 2003*b*). Heterogeneous displacements in this geometry introduce an additional degree of complexity. According to the linear stability analysis of radial displacements (Tan & Homsy 1987; Riaz & Meiburg 2003*a*), the wavenumber of the most amplified azimuthal viscous instability mode remains constant as the front moves away from the source. Consequently, the instability

wavelength changes continuously as a function of the radial distance from the source, so that the ratio of the permeability to the viscous length scale, and thereby the potential for resonance, change continuously over time. Chen & Meiburg (1998*b*) conduct a detailed investigation of the coupling between viscous and permeability related vorticity for two-dimensional quarter five-spot displacements using a correlated random permeability field. How this coupling is modified in three dimensions, and in the presence of buoyancy effects, is to be investigated here.

The identification of different flow regimes in heterogemeous displacements has been the subject of several earlier investigations, among them those of Waggoner *et al.* (1992), Sorbie *et al.* (1992) and Kempers & Haas (1994). According to these authors the variable-viscosity flow in a nearly homogeneous reservoir with little dispersion is termed 'viscous fingering', while a nearly constant-viscosity displacement dominated by strong heterogeneity is referred to as 'channelling'. Finally, displacements dominated by mechanical dispersion are said to be in the 'dispersive regime'. In the present investigation, our goal is to analyse the vorticity interaction mechanisms for these kinds of flows, and for the parameter ranges where transitions between these regimes occur. Towards this end, we will compare the natural nonlinear wavelength of homogeneous flows with corresponding wavelengths of heterogeneous displacements.

The paper is organized as follows. Section 2 describes the physical model and the governing equations. In § 3, we begin our analysis by addressing the conceptually simple problem of two-dimensional displacements in the presence of periodic permeability variations. By analysing the characteristic wavenumbers and the norms of the various vorticity contributions, we are thus able to establish the different regimes of viscous fingering, resonant amplification, and dispersion. We subsequently apply the insight gained from the periodic permeability fields to random heterogeneity distributions. These give rise to a range of permeability length scales, which renders the interactions with the viscous instability more complex. Neutrally buoyant three-dimensional displacements are discussed in § 4, while § 5 addresses three-dimensional displacements with gravity override. The main conclusions from the present investigation are summarized in § 6.

2. Governing equations

The mathematical model, described in detail by Riaz & Meiburg (2003*b*), is based upon the vorticity formulation of Darcy's equation. We assume incompressible flow and use a convection–diffusion equation to advance the concentration field of the injected fluid. The computational domain is shown in figure 1. In order to derive the dimensionless equations, we choose the side length L of the domain as the characteristic length scale. By denoting the source strength per unit depth as $2\pi Q$, we thus obtain time and velocity scales as L^2/Q and Q/L, respectively. The viscosity μ_1 of the injected fluid is taken as the reference value for scaling the viscosities, while the difference in the fluid densities $\rho_2 - \rho_1$ provides a characteristic density value. Here the index '1' refers to the injected fluid, while '2' denotes the displaced fluid. We define an aspect ratio $A = H/L$, where H is the domain height. The resulting governing equations in non-dimensional form are

$$\nabla \cdot \boldsymbol{u} = 0, \tag{2.1}$$

$$\omega = \frac{1}{k}\nabla k \times \boldsymbol{u} + R\nabla c \times \boldsymbol{u} + \frac{G\,k}{\mu}\nabla c \times \hat{\boldsymbol{e}}_z, \tag{2.2}$$

$$\frac{\partial c}{\partial t} + \boldsymbol{u} \cdot \nabla c = \frac{1}{Pe}\nabla^2 c, \tag{2.3}$$

where $\hat{\boldsymbol{e}}_z$ is the unit vector in the z-direction. For simplicity, we will refer to the terms on the right-hand side of the vorticity equation as 'permeability vorticity', 'viscous vorticity', and 'gravitational vorticity', respectively. Three dimensionless parameters appear in the above equations: the Péclet number Pe, the gravity parameter G, and the viscosity ratio parameter R

$$Pe = \frac{Q}{D}, \tag{2.4}$$

$$G = \frac{g(\rho_2 - \rho_1)KL}{Q\mu_1}, \tag{2.5}$$

$$R = -\frac{1}{\mu}\frac{\mathrm{d}\mu}{\mathrm{d}c} = \ln\left(\frac{\mu_2}{\mu_1}\right). \tag{2.6}$$

Here, c denotes the concentration of the injected fluid, and k represents the locally varying isotropic permeability; K indicates the average of the permeability field, which is taken as the characteristic permeability value; μ and ρ are the concentration-dependent viscosity and density, expressed as

$$\mu = \mathrm{e}^{R(1-c)},$$

$$\rho = \frac{\rho_2}{\rho_2 - \rho_1} - c.$$

We take the scalar diffusion coefficient to be a constant D.

The velocity is obtained through a three-dimensional vector potential (Fletcher 1991) as

$$\boldsymbol{u} = \nabla \times \psi, \tag{2.7}$$

$$\nabla^2 \psi = -\omega. \tag{2.8}$$

At the vertical boundaries symmetry conditions are assumed, while the top and bottom represent no-flux boundaries. By denoting the spatial components of ψ and ω as $(\phi,\ \theta,\ \chi)$ and $(\xi,\ \sigma,\ \zeta)$, respectively, we thus obtain

$$x = 0, 1 : \begin{cases} c_x = 0, & k_x = 0, & \\ u = 0, & v_x = 0, & w_x = 0, \\ \phi_x = 0, & \theta = 0, & \chi = 0, \\ \xi_x = 0, & \sigma = 0, & \zeta = 0, \end{cases} \tag{2.9}$$

$$y = 0, 1 : \begin{cases} c_y = 0, & k_y = 0, & \\ u_y = 0, & v = 0, & w_y = 0, \\ \phi = 0, & \theta_y = 0, & \chi = 0, \\ \xi = 0, & \sigma_y = 0, & \zeta = 0, \end{cases} \tag{2.10}$$

$$z = 0, A : \begin{cases} c_z = 0, & k_z = 0, & w = 0, \\ \phi = 0, & \theta = 0, & \chi_z = 0. \end{cases} \tag{2.11}$$

In order to avoid an initially singular concentration distribution, we specify as the initial condition at a small but finite time the self-similar concentration profile corresponding to the radially symmetric problem (Tan & Homsy 1987). It has the form

$$c_o = \frac{1}{2}\left[1 + \mathrm{erf}\left(\sqrt{Pe}\left(\frac{r}{r_o} - 1\right)\right)\right]. \tag{2.12}$$

Here r_o represents the initial radial location of the front. It determines the 'effective starting time' $t_0 > 0$ of the computation as

$$t_0 = 0.5\, r_o^2, \tag{2.13}$$

The above equations are solved computationally by a combination of the Fourier–Galerkin spectral method (Gottlieb & Orszag 1977; Canuto *et al.* 1986) and sixth-order compact finite differences (Lele 1992), in conjunction with an explicit third-order time-stepping scheme. Numerical simulations are performed with very high resolutions in order to resolve all relevant length scale. Runtimes can vary between 10 hours for two-dimensional (single processor) and 2 days for three-dimensional (multiple processor) calculations on an SGI – Origin machine. A more detailed discussion of the governing equations, numerical method and parallelization procedure is provided by Riaz & Meiburg (2003*b*) and Riaz (2003).

3. Two-dimensional displacements

We begin by analysing displacements through a spatially periodic permeability field. This will enable us to identify some of the basic dynamical mechanisms associated with heterogeneous displacements. The insight gained from this conceptually simple permeability field will subsequently be utilized to study the more complex situation of displacements in random permeability fields. In the discussion of heterogeneous displacements, the natural length scale of the viscous instability in a *homogeneous* displacement will play a key role, so that it will be discussed first.

3.1. *Natural viscous length scale of homogeneous displacements*

To identify the dominant length scale in nonlinear displacements, we evaluate the characteristic wavenumber of the vorticity field associated with viscosity variations. An effective wavenumber $\tilde{n}$ is defined as

$$\tilde{n} = \frac{\displaystyle\int_0^{\tilde{K}} \tilde{k} E(\tilde{k})\, \mathrm{d}\tilde{k}}{\displaystyle\int_0^{\tilde{K}} E(\tilde{k})\, \mathrm{d}\tilde{k}}, \tag{3.1}$$

where $\tilde{k}$ is the wavenumber associated with the Fourier decomposition of the vorticity field and $E(\tilde{k})$ is the energy spectrum of the vorticity field; $\tilde{n}$ is the dominant wavenumber of the displacement. It becomes $\tilde{n}_h$, $\tilde{n}_v$ or $\tilde{n}_p$ when the vorticity field it is associated with is viscous homogeneous, viscous heterogeneous or permeability, respectively.

We briefly examine the evolution of the characteristic wavenumber $\tilde{n}_h$ of the viscous vorticity field for homogeneous displacements. Figure 2 shows $\tilde{n}_h$ along with the most amplified mode given by the linear stability analysis of the equivalent radially symmetric situation at identical times, for various Péclet numbers (Tan & Homsy 1987; Riaz & Meiburg 2003*a*). There is remarkably good agreement, especially for higher Péclet numbers and for early times. Note that the slope of $\tilde{n}_h$ for $Pe = 200$ and 400 closely follows the $1/\sqrt{2t}$ behaviour of the linear stability results, which indicates a weak effect of the nonlinearity on the dominant wavenumber. For the larger Péclet numbers of $Pe = 800$ and 1200, the nonlinear fingering interactions lead to a more substantial deviation from the linear behaviour. Note that we have found $\tilde{n}_h$ to be largely independent of the specific random initialization of concentration

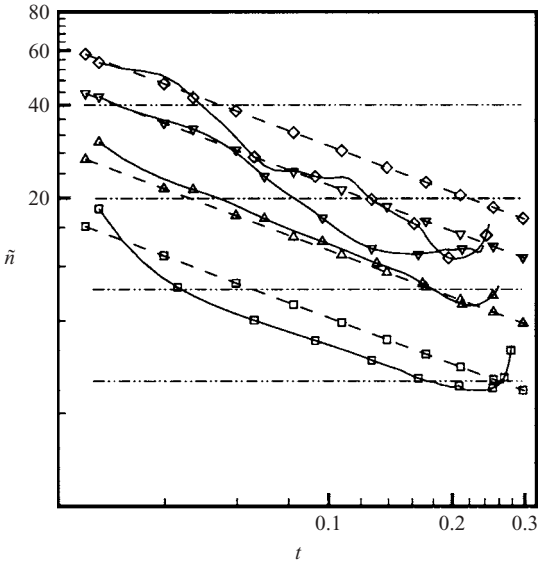

FIGURE 2. Comparison between the characteristic wavenumber of homogeneous displacements $\tilde{n}_h$ obtained from two-dimensional nonlinear simulations (solid lines), and the most amplified wavenumber from the linear stability analysis of the corresponding radially symmetric base flow profiles (dashed lines), for various Péclet numbers. The horizontal dash-dotted lines indicate the permeability wavenumbers considered in the present work. □, $Pe = 200$; △, $Pe = 400$; ▽, $Pe = 800$; ◇, $Pe = 1200$.

perturbations. The figure not only provides some measure of validation of the computational results, but it also gives the most amplified nonlinear mode of the freely developing viscous instability as a reference for the subsequent discussion of heterogeneous displacements. There we will find that the closer the value of the viscous vorticity wavenumber $\tilde{n}_v$ for heterogeneous displacements is to $\tilde{n}_h$ for homogeneous displacements, the higher the possibility of a resonant amplification. Conversely, the potential for amplification diminishes with a deviation of $\tilde{n}_v$ from $\tilde{n}_h$.

3.2. *Spatially periodic permeability field*

A spatially periodic permeability field is specified as

$$k(x, y) = \exp\{\gamma \cos(2\pi l x) \cos(2\pi m y)\}, \tag{3.2}$$

where the wavenumbers l and m are the inverse of the correlation lengths in the x- and y-directions, respectively. Unless specified otherwise, we take l and m to be equal. The standard deviation γ is the square root of the variance s of the permeability field.

Typical displacements through spatially periodic permeability fields are displayed in figure 3. Concentration plots of the injected fluid serve to visualize the interface. Figures 3(a) and 3(b) show the contours at two different times for the small wavenumber of $m = 5$. The fingers are seen to develop along high permeability paths mainly around the diagonal. A higher wavenumber $m = 20$ is shown in figures 3(c) and 3(d). Here more fingers are generated, with a layered structure along the diagonal. In order to analyse the above displacement processes quantitatively, we

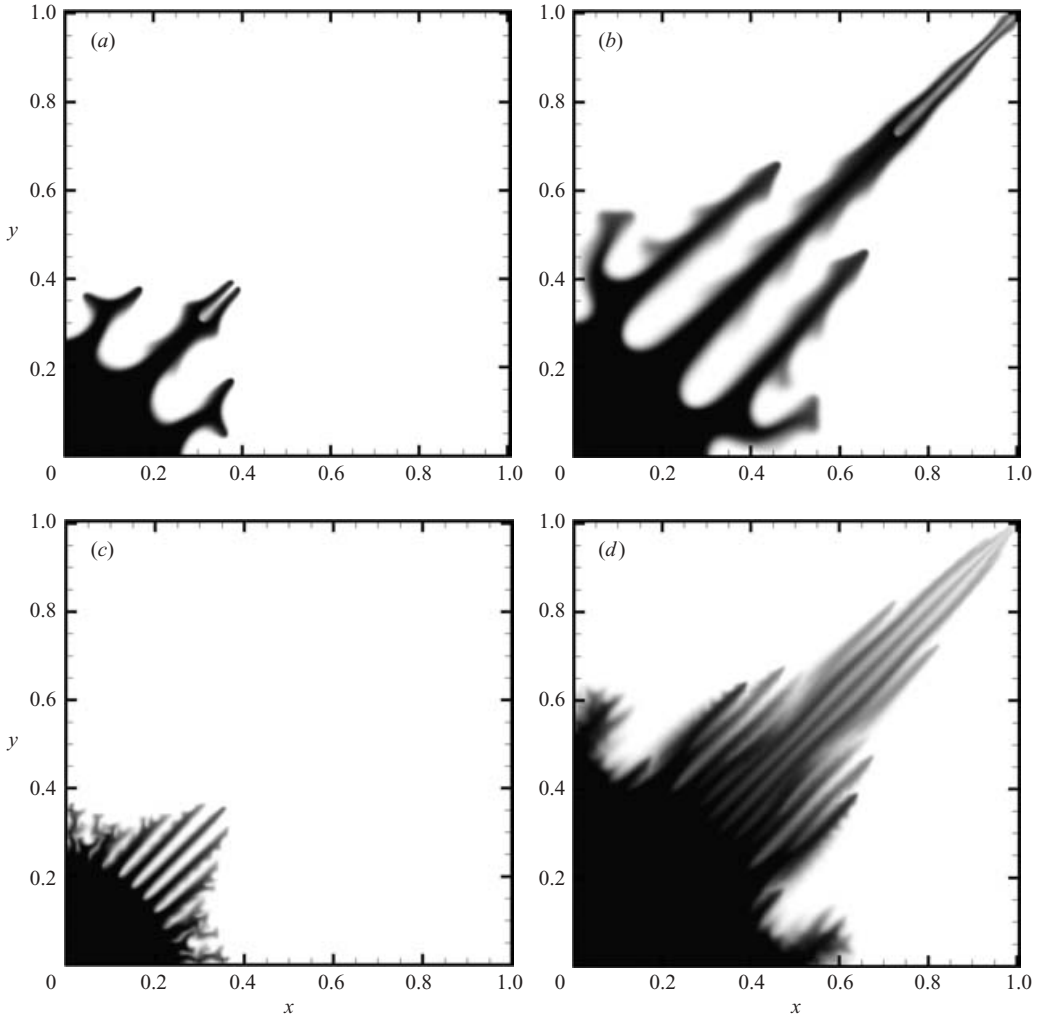

FIGURE 3. Concentration fields for displacements in spatially periodic permeability distributions. $Pe = 800$, $R = 2.5$, $s = 0.5$. (*a*) $m = 5$, $t = 0.1$, (*b*) $m = 5$, $t = 0.127$, (*c*) $m = 20$, $t = 0.1$, (*d*) $m = 20$, $t = 0.144$. As explained in the text, for $m = 5$ an initial viscous fingering dominated phase is followed by a resonant amplification phase. For $m = 20$, an initial resonant amplification phase gives way to a dispersive phase during which the interface slows down, thereby enhancing the displacement efficiency.

introduce the norm of the viscous and permeability vorticity fields, respectively:

$$\|\omega_v(t)\| = \sqrt{\frac{1}{L\,M}\sum_{i=1}^{L}\sum_{j=1}^{M}\omega_v(t)_{i,j}^2}, \quad \omega_v = R\nabla c \times \boldsymbol{u}, \tag{3.3}$$

$$\|\omega_p(t)\| = \sqrt{\frac{1}{L\,M}\sum_{i=1}^{L}\sum_{j=1}^{M}\omega_p(t)_{i,j}^2}, \quad \omega_p = \frac{1}{k}\nabla k \times \boldsymbol{u}. \tag{3.4}$$

Here L and M denote the number of computational grid points in the x- and y-directions, respectively. Figure 4 shows the viscous vorticity norm for $R = 2.5$,

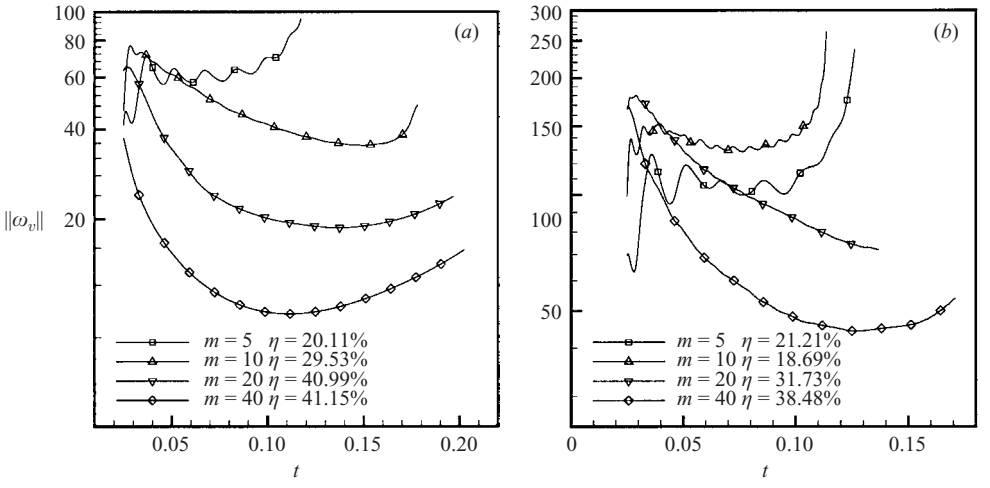

FIGURE 4. Viscous vorticity norm for various values of the correlation wavenumber m, with $R = 2.5$ and $s = 0.5$ in the spatially periodic permeability field: (*a*) $Pe = 200$, (*b*) $Pe = 800$. The maximum value of the norm at early times reflects the initial amplification of the viscous vorticity at certain values of m. As explained in the text, the sustained growth for lower values of m at late times is due to a resonant amplification, while the steep decay of the norm for larger m indicates the dispersive regime.

$s = 0.5$, and various permeability correlation lengths, at two values of Pe. Pronounced differences are noticeable among the various simulations with respect to the evolution of the viscous vorticity norm. While in some simulations a significant growth of the vorticity norm occurs for either early or late times, other displacements are characterized by long phases during which the vorticity norm declines. Generally, a higher overall vorticity level is indicative of a more vigorous evolution of the displacement front, which in turn results in an earlier breakthrough. Here the breakthrough time t_b is defined as the time when the concentration of the injected fluid first reaches 1% somewhere along the height of the production well. Correspondingly, the overall efficiency η of the displacement process is given as the fraction of the total domain volume occupied by the injected fluid at the time of breakthrough, $\eta = \pi t_b/2$.

In order to gain insight into the mechanisms governing this overall vorticity evolution, it is instructive to analyse the dominant length scales of the viscous and permeability vorticity fields, and to compare them with the natural length scale of the corresponding homogeneous displacement. This information is contained in figure 5, which displays the characteristic wavenumbers of the viscous ($\tilde{n}_v$) and permeability ($\tilde{n}_p$) vorticities, for the same set of simulations as in figure 4. In figure 5 $\tilde{n}_p$ is seen to remain nearly constant throughout the displacement process, as the permeability field does not change. The natural wavenumbers of the corresponding homogeneous displacements $\tilde{n}_h$ are shown by thick solid lines. As discussed above, they decrease with time, due to the self-similar evolution of the interface, as well as the nonlinear mechanisms of merging, coalescence and shielding in radial base flows (Tan & Homsy 1987; Chen & Meiburg 1998*a*).

If the natural length scale of the corresponding homogeneous case lies substantially above that of the permeability field, figure 5 indicates that in the heterogeneous displacement the dominant scale of the viscous vorticity remains close to the permeability length scale. Waggoner *et al.* (1992) term this effect *dispersive*. In this

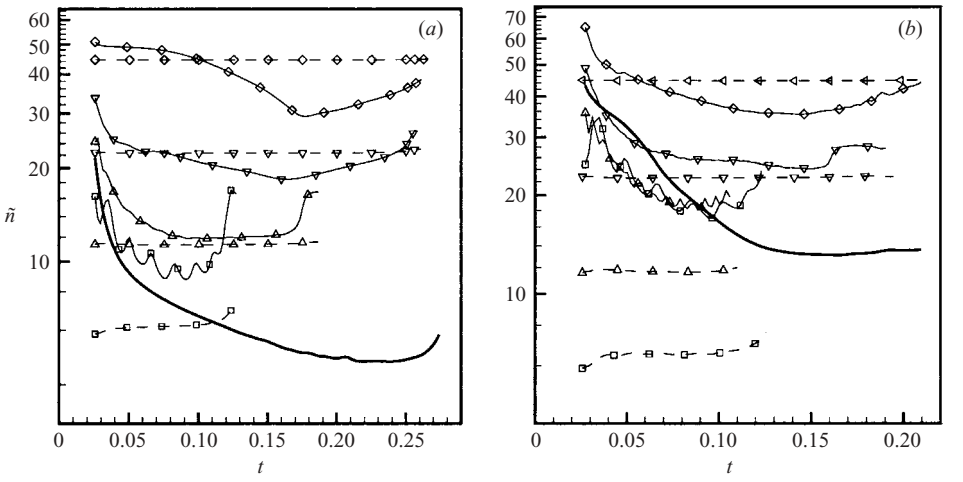

FIGURE 5. The characteristic wavenumbers of the viscous ($\tilde{n}_v$, solid line) and permeability ($\tilde{n}_p$, dashed line) related vorticities for the spatially periodic permeability fields at $R = 2.5$, $s = 0.5$ and various values of m. □, $m = 5$; △, $m = 10$; ▽, $m = 20$; ◇, $m = 40$. (*a*) $Pe = 200$, (*b*) $Pe = 800$. The thick line shows the natural wavenumber $\tilde{n}_h$ for the corresponding homogeneous case. Harmonic resonance at an early time of $t = 0.03$ is indicated by $\tilde{n}_v \approx \tilde{n}_h$ and $\tilde{n}_v \approx 2\tilde{n}_p$ for $m = 10$ and $m = 20$ in (*a*) and (*b*), respectively. The dispersive regime occurs when either $\tilde{n}_v \gg \tilde{n}_h$ or $\tilde{n}_v < \tilde{n}_p$. At a later time $t > 0.05$, the $m = 5$ case in (*a*), and the $m = 5$ and 10 cases in (*b*) undergo harmonic resonance.

regime, the viscous instability can no longer evolve at its natural wavelength, as it is constrained by the length scale of the permeability field. Consequently, dispersion gains importance and reduces the overall concentration gradients (figure 3*d*), so that the interface advances at a slower rate. This is reflected by a damping of $||\omega_v||$ at later times for those displacements with natural length scale larger than the permeability length scale, e.g. $m = 10$, 20, and 40 in figure 4(*a*), and $m = 20$ and 40 in figure 4(*b*).

If the natural length scale initially is smaller than the permeability correlation length, the viscous instability is free to grow at its natural scale for early times, i.e. $\tilde{n}_v \approx \tilde{n}_h$. Figure 5(*a*) shows that this is the case at $Pe = 200$ for $m = 5$ and $m = 10$. The subsequent increase of this natural wavelength brings the viscous length scale closer to that of the permeability, so that the vorticity can undergo a resonant amplification. This harmonic resonance was established by means of a linear stability analysis for rectilinear heterogeneous displacements (De Wit & Homsy 1997*a*) and observed for nonlinear displacements by De Wit & Homsy (1997*b*), Chen & Meiburg (1998*b*) and Camhi *et al.* (2000). Examples can be found in the early vorticity growth around $t = 0.03$ for $Pe = 200$ and $m = 10$, or for $Pe = 800$ and $m = 20$, when $\tilde{n}_v \approx 2\tilde{n}_p$. This resonant amplification of the viscous vorticity by the first harmonic of $\tilde{n}_p$ causes the highest early values of $\|\omega_v\|$ to appear for an intermediate permeability length scale. For the $m = 5$ case shown in figure 5(*a*), $\tilde{n}_v$ follows $\tilde{n}_h$ closely until $t \approx 0.05$. Thereafter it maintains a value of $\approx 2\tilde{n}_p$ until just before breakthrough, again allowing a resonant interaction. This is reflected by the sustained high level of $\|\omega_v\|$. Similar situations occur for the cases of $m = 5$ and 10 at $Pe = 800$ in figures 4(*b*) and 5(*b*). The displacement efficiency values noted in figure 4 show that these late-time amplifications result in the least efficient processes for $m = 5$ and $Pe = 200$, and for $m = 10$ and $Pe = 800$. For large values of m, an increase in the viscous vorticity at later time, as shown in figures 4(*a*) and 4(*b*), indicates that the dominance of dispersion and

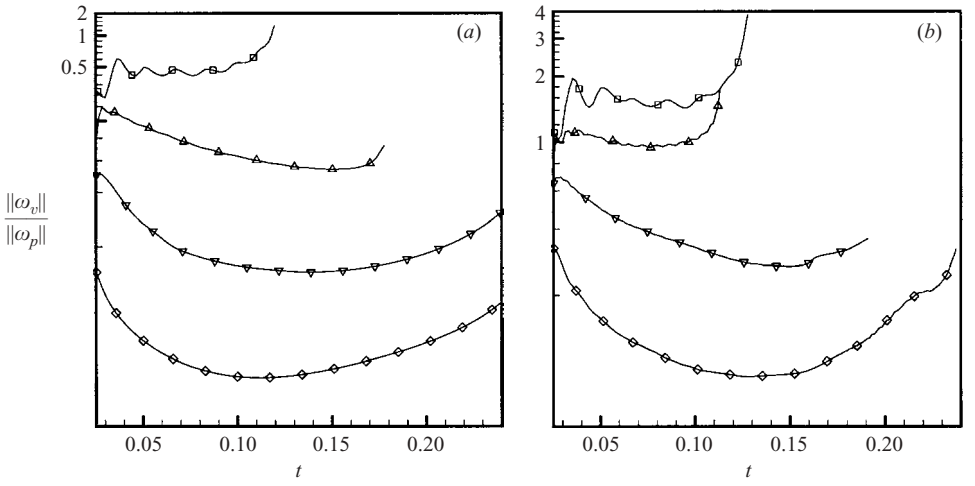

FIGURE 6. Ratio of the norms of the viscous and permeability vorticity. (*a*) $Pe = 200$, (*b*) $Pe = 800$. □, $m = 5$; △, $m = 10$; ▽, $m = 20$; ◇, $m = 40$. A comparison with figure 5 indicates that in the viscous fingering regime $\|\omega_v\|/\|\omega_p\| > 1$, while in the dispersive regime $\|\omega_v\|/\|\omega_p\| < 1$. Resonant amplification occurs when $\|\omega_v\|/\|\omega_p\| \approx 1$.

finger interaction lead to the generation of large-scale structures which are relatively unaffected by small-scale permeability variations and can again move rapidly towards the production well. This effect will be seen to become more important for three-dimensional displacements.

Figures 4 and 5 reflect the existence of three basic parameter regimes for heterogeneous displacements, which can be summarized as follows:

$$\text{viscous fingering} : \tilde{n}_v \approx \tilde{n}_h \quad \text{and} \quad \tilde{n}_v > \tilde{n}_p, \tag{3.5}$$

$$\text{resonant amplification} : \tilde{n}_v \approx \tilde{n}_h \quad \text{and} \quad \tilde{n}_v \approx i\,\tilde{n}_p, \quad i = 1, 2, \ldots, \tag{3.6}$$

$$\text{dispersive} : \tilde{n}_v \gg \tilde{n}_h. \tag{3.7}$$

The physical mechanism of amplification can be understood as follows. As the viscous fingers develop due to variations in permeability, viscous vorticity dipole structures (see De Wit & Homsy 1997*a* and Chen & Meiburg 1998*a*) are generated along the sides of the fingers. They increase the flow of less viscous fluid through the fingers, thereby increasing the local velocity. This increase in velocity serves to increase the permeability vorticity, which in turn further amplifies the local velocity and the viscous vorticity. When the viscous and permeability vorticity dipole structures are close to each other or in a certain spatial relationship, the viscous vorticity can be substantially amplified, leading to the resonance phenomenon. The dispersive behaviour occurs when the width of the viscous finger is larger than the channel width, such that the permeability vorticity accelerates only a small portion of the less viscous fluid inside the finger. This leads to mechanical dispersion of the viscous finger.

Figure 6 shows the ratio $||\omega_v||/||\omega_p||$ of the viscous and permeability vorticity norms. It demonstrates that the resonant amplification cases of $m = 5$, $Pe = 200$ and $m = 10$, $Pe = 800$ are associated with $||\omega_v||/||\omega_p|| \approx 1$. In this way, the viscous and permeability vorticities are in an approximate balance, so that they can optimally feed upon each other. The viscous fingering regime typically has $||\omega_v||/||\omega_p|| > 1$, so

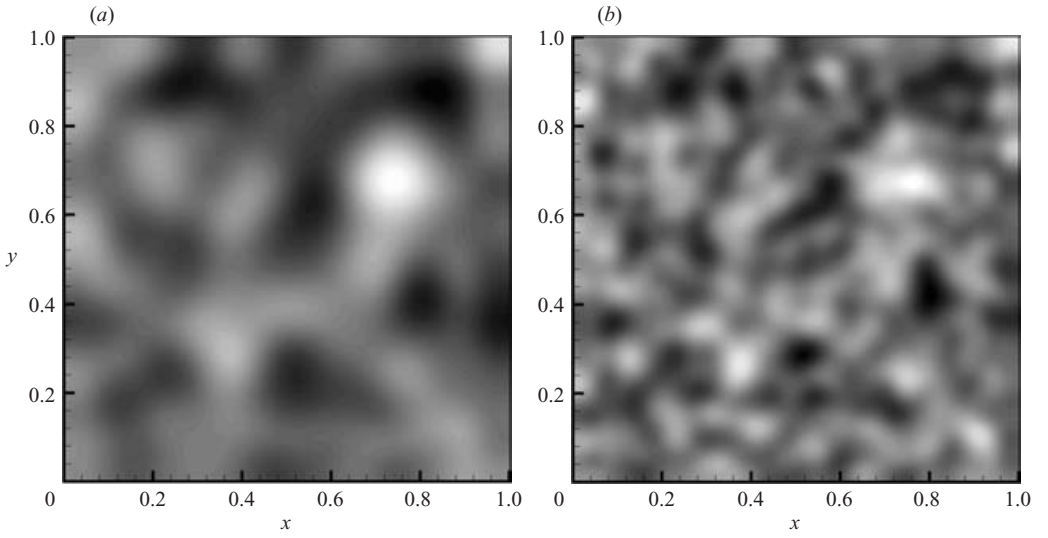

FIGURE 7. Random permeability distribution. (*a*) $l = m = 5$, (*b*) $l = m = 20$. The random permeability field is characterized by a wavenumber spectrum whose band width is specified by the correlation numbers l and m.

that it is dominated by viscosity effects. On the other hand, the dispersive case is characterized by $||\omega_v||/||\omega_p|| < 1$, i.e. permeability effects dominate.

3.3. *Random permeability*

The knowledge gained from analysing flows in periodic permeability fields can now be employed in studying the more complex situation of displacements through random permeability fields. In order to construct such a random permeability field with a given variance and correlation length, we follow the approach by Tan & Homsy (1992). We define a correlation function

$$R_f(x, y) = s\ \exp[-\pi\{(x\,l)^2 + (y\,m)^2\}], \tag{3.8}$$

where l and m are the wavenumbers in the x- and y-directions, respectively, and s denotes the variance of the permeability field. The spectral transform of the correlation function R_f provides the probability density function, which is then used to construct a random field f with a variance of s and mean of 0, according to an algorithm given by Shinozuka & Jen (1972). The permeability field k is then specified as $k = \mathrm{e}^f$. Contour profiles of the random permeability fields for $l = m = 5$ and $l = m = 20$, respectively, are shown in figure 7. Unless otherwise noted, l and m will be equal. In order to impose the condition of vanishing derivatives normal to the boundaries, we employ the approach of Chen & Meiburg (1998*b*) and Camhi *et al.* (2000). Statistically, the random field f has a Gaussian distribution, whose spread is controlled by the variance. Note that the random heterogeneity is characterized by a wavenumber spectrum, rather then a pure mode, which was the case for a periodic permeability distribution. As a result, the complexity of the coupling between the viscous and permeability vorticity components increases significantly, in view of the fact that the spectrum of unstable modes can now be excited at different levels by the permeability spectrum, particularly for large values of Pe, R and m. In other words, larger m, Pe or R values increase the ability of the permeability variations to induce resonant amplification at different length scales due to the excitation mechanisms

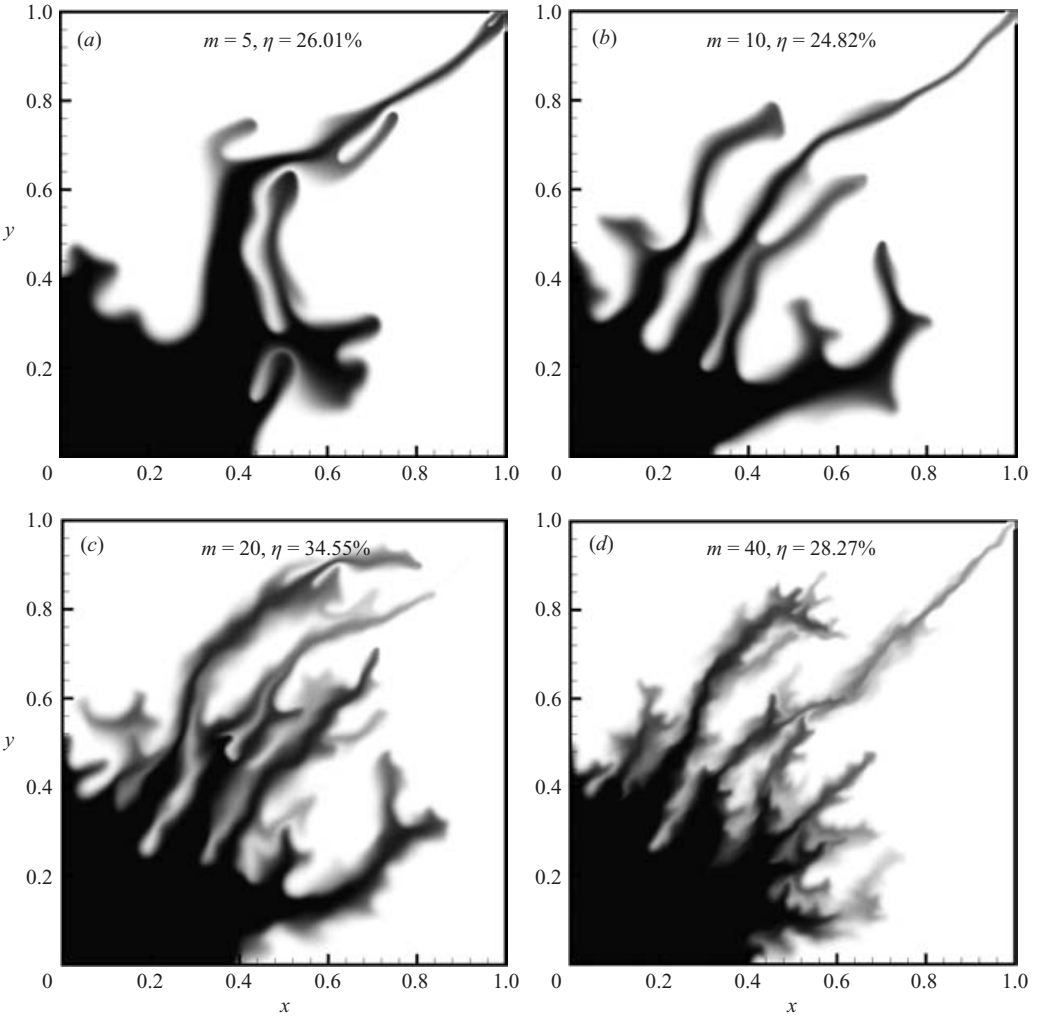

FIGURE 8. Concentration fields for displacements in random permeability distributions with $Pe = 800$, $R = 2.5$, and $s = 0.5$. The variation in the breakthrough efficiency η as a function of m highlights the strong influence of the random distribution of high permeability paths in the domain.

related to harmonic and subharmonic resonances. The most significant amplification of viscous vorticity is expected to occur close to the most amplified naturally occurring mode in homogeneous displacements.

In the light of the above discussion, we will briefly revisit two-dimensional quarter five-spot displacements (Chen & Meiburg 1998*b*), in order to establish the extent to which the concepts developed from the study of periodic heterogeneities can be extended to the random heterogeneity case. Subsequently, we will proceed to the investigation of three-dimensional displacements.

3.3.1. *Influence of the permeability wavenumber*

Figure 8 shows the concentration contours for displacements in random heterogeneous permeability fields of various wavenumbers m, at $Pe = 800$, $R = 2.5$ and $s = 0.5$. For a small wavenumber ($m = 5$, figure 8*a*), the permeability field offers

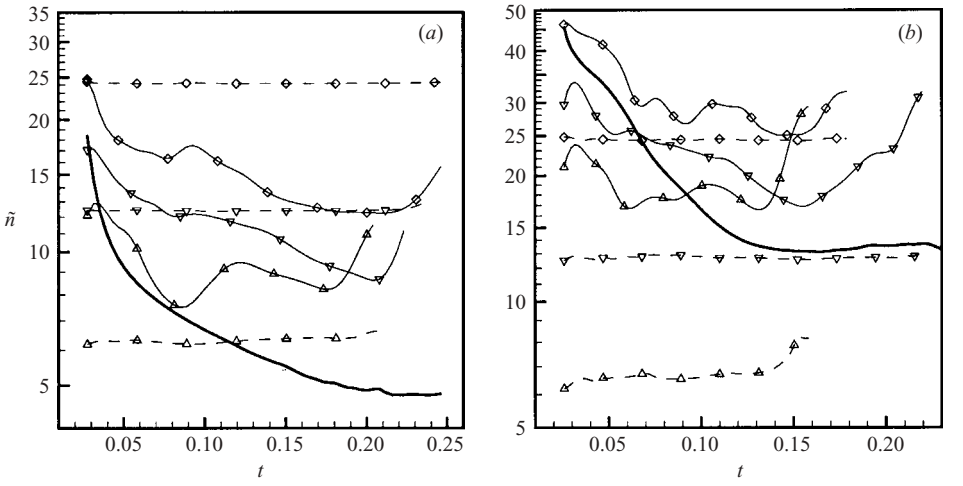

FIGURE 9. Characteristic wavenumbers of the viscous ($\tilde{n}_v$, solid line) and permeability ($\tilde{n}_p$, dashed line) vorticities in random permeability fields for $R = 2.5$, $s = 0.5$, and various values of m. (*a*) $Pe = 200$, (*b*) $Pe = 800$. $\triangle$, $m = 10$; $\triangledown$, $m = 20$; $\diamond$, $m = 40$. Various regimes can be identified based on the criteria (3.5), (3.6) and (3.7).

a limited choice of high-permeability paths, so that the front is forced to follow the circuitous route towards the sink. For the $m = 10$ case shown in figure 8(*b*), the existence of several high-permeability paths close to the diagonal allows the front to adopt a straighter path towards the sink, and thereby to achieve an earlier breakthrough. However, this trend of having the dominant finger closer and closer to the diagonal as m increases, is not uniform. For $m = 20$ (figure 8*c*), an off-diagonal path is dominant again, even though several high-permeability paths exist close to the diagonal. For $m = 40$, figure 8(*d*), we observe a wide range of length scales. In this case, an off-diagonal path is again the most developed one. Note that all four of the permeability fields were generated with the same set of random numbers, which explains the similarity among them as far as the large scales are concerned.

In order to gain insight into the interaction mechanisms dominating these displacements at $Pe = 800$, we analyse the characteristic wavenumbers of the viscous and permeability vorticities for $R = 2.5$ and $s = 0.5$, shown in figure 9. For comparison, the corresponding data for $Pe = 200$ are shown as well. Note that, since the $\tilde{n}_p$ values represent a weighted average of the spectrum, they are generally somewhat smaller than the corresponding values of m, which specify the bandwidth of the permeability spectrum. These data indicate whether the displacements are dominated by viscous fingering, resonant amplification, or dispersion.

For $Pe = 200$ a resonant amplification is indicated for $m = 40$ by $\tilde{n}_v \approx \tilde{n}_p$, shown in figure 9(*a*). Thereafter, the viscous wavenumber drops rapidly below the permeability wavenumber indicating a dispersion-dominated behaviour. For $m = 10$, the dominant wavenumber $\tilde{n}_v$ follows the homogeneous curve until it almost reaches the permeability wavenumber $\tilde{n}_p$ at $t \approx 0.09$. The subsequent steep increase to a higher wavenumber is possibly triggered by a resonant amplification.

For $Pe = 800$, the $m = 40$ case undergoes a resonant amplification with $\tilde{n}_v \approx 2\tilde{n}_p$ at early times, and with $\tilde{n}_v \approx \tilde{n}_p$ for $0.07 < t < 0.12$, as seen in figure 9(*b*). Subsequently, dispersive behaviour occurs with $\tilde{n}_v \approx \tilde{n}_p$. Harmonic resonance ($\tilde{n}_v \approx 2\tilde{n}_p$) is also observed for $m = 20$ during the time interval $0.05 < t < 0.09$, and for $m = 10$ around

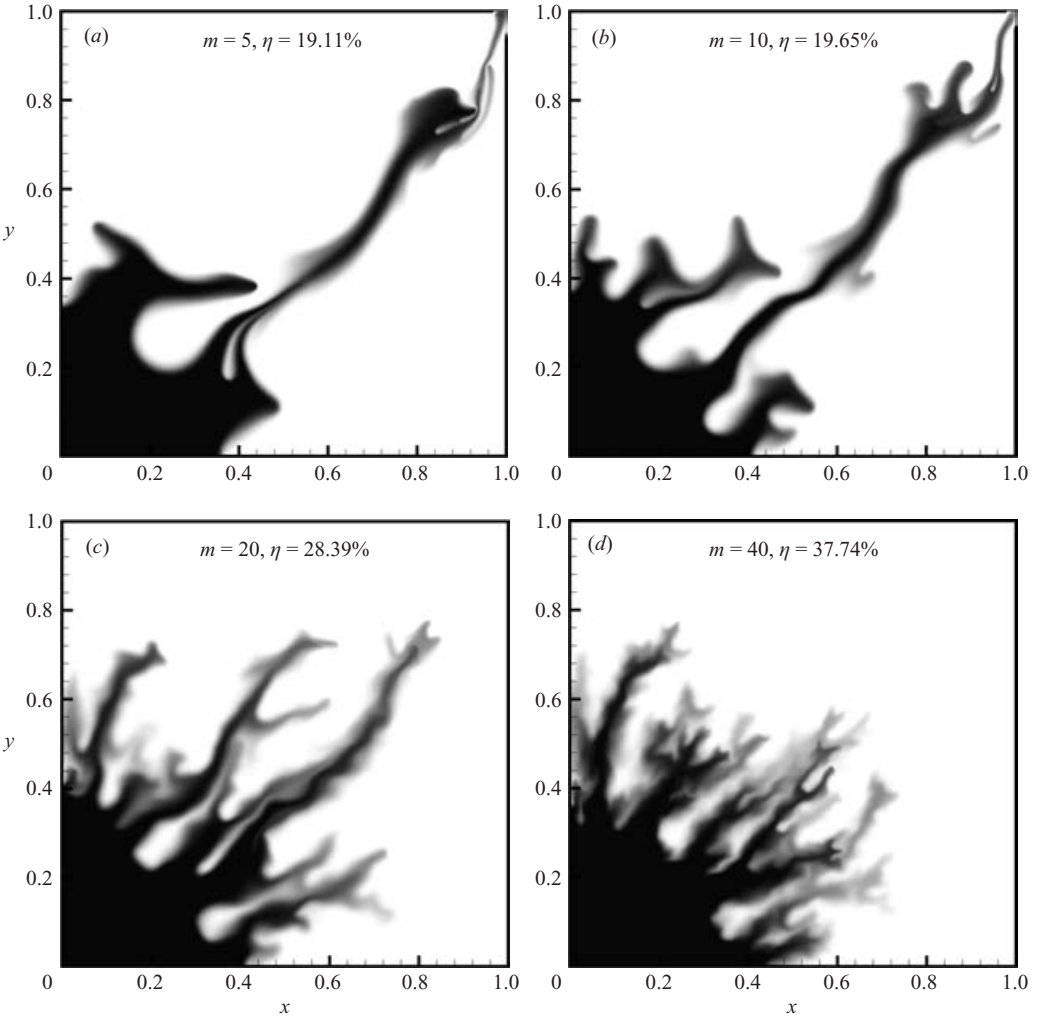

FIGURE 10. Concentration contours for the same flow parameters as in figure 8 ($Pe = 800$, $R = 2.5$, $s = 0.5$), but different random permeability fields. Displacements in these fields give rise to breakthrough efficiencies that grow monotonically with m.

$t = 0.1$ ($\tilde{n}_v \approx 3\,\tilde{n}_p$). The concentration contour plot for $m = 20$ in figure 8(c) suggests that the early-time resonant amplification leads to a rapid development of fingers away from the diagonal.

3.3.2. *Influence of random realization*

The above analysis of displacements through random permeability fields demonstrates the strong influence of the correlation length on the level of coupling between the viscous and permeability vorticities. We now investigate the sensitivity to individual random realizations of the permeability field. Figure 10 shows the concentration contours for the same flow parameters as in figure 8, but for permeability fields obtained from a different set of random numbers. Note that all four permeability fields shown in figure 10 were generated with the same set of random numbers (just as all four fields of figure 8 were), even though they have different correlation

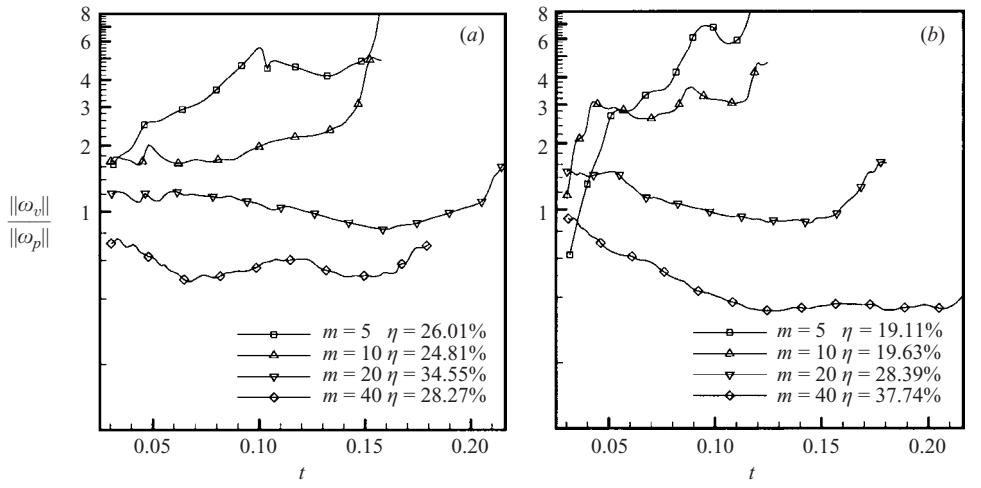

FIGURE 11. Ratio of the viscous and permeability related vorticity norms for the random fields used in (*a*) figure 8 and (*b*) in figure 10. The ratios are largely independent of the random realization. However, note that the transition to the dispersive regime occurs at a larger value of m for random heterogeneity fields, as compared to the periodic heterogeneity shown in figure 6. The harmonic resonance regime at $m = 20$ for the two random cases, despite similar values of $||\omega_v||/||\omega_p||$, leads to very different displacement efficiencies. However, for the viscous fingering ($m = 5$ and 10) and dispersive ($m = 40$) regimes, the displacement efficiency is more clearly correlated to the ratio of the norms, such that higher values of $||\omega_v||/||\omega_p||$ result in a lower efficiency.

lengths. For this reason, all four fields shown in each of these plots share similar large-scale features. However, while figure 8 had indicated a maximum efficiency for the intermediate correlation wavenumber of $m = 20$, figure 10 displays a monotonic increase of the efficiency with m. Inspection of the concentration contours shows that this behaviour is directly related to the spatial distribution of high-permeability regions in the domain. The permeability fields employed in figure 10 offer low-resistance paths mainly along the diagonal. For increasing values of m, the growing ratio of viscous to permeability length scale leads to more dispersive effects and higher displacement efficiency.

3.3.3. *Relative strengths of the viscous and permeability vorticity fields*

Analysing the magnitudes of the viscous and permeability vorticity norms can shed additional light on the mechanisms dominating different parameter regimes. Figure 11 shows the ratio $\|\omega_v\|/\|\omega_p\|$ to be quite similar for the two sets of displacements depicted in figures 8 and 10. For $m = 5$ and 10, this ratio is substantially larger than one, indicating the viscous fingering regime. The resonant amplification for $m = 20$ leads to a ratio near unity, and the dispersive regime for $m = 40$ is reflected by a ratio consistently smaller than one. We observe that for the resonant amplification regime very similar values of $\|\omega_v\|/\|\omega_p\|$ can lead to substantially different breakthrough efficiencies for the two $m = 20$ cases shown in figures 6(*a*) and 6(*b*).

Note that the above information is based on spectra, and therefore in a sense describes spatially averaged information. It is to be kept in mind that the resonant amplification between viscous and permeability vorticity can of course happen in localized areas of the flow field.

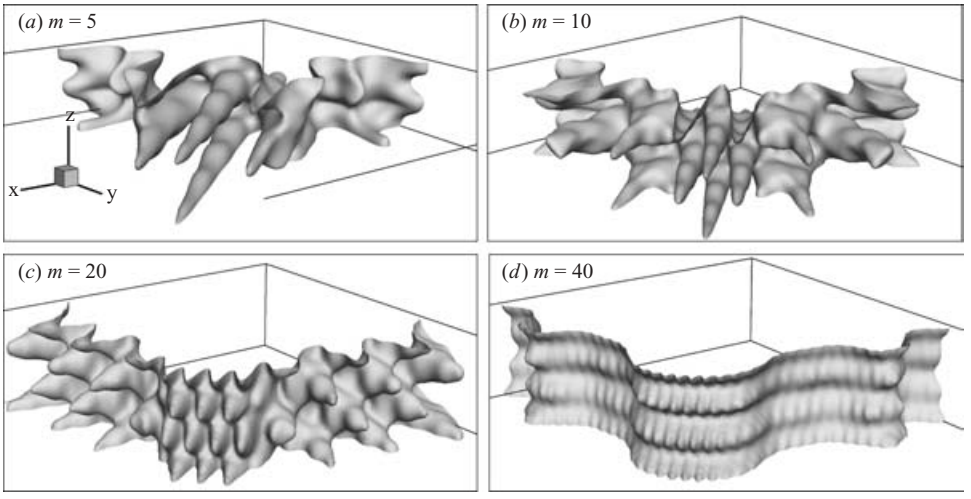

FIGURE 12. Concentration isosurfaces for $Pe = 400$, $R = 2.5$, $G = 0$, $A = 1/8$, $s = 0.1$, $n = 12$ and various values of m at $t = 0.14$. For $m = 5$ and 10, the diagonal regions exhibit well-developed fingers, while the off-diagonal areas show some large-scale structures as a result of merging events. Larger values of m tend to reduce the finger amplitude through dispersion. The dispersion-dominated displacement for $m = 40$ smooths out small-scale fingers, and instead gives rise to a large-scale horizontal wave.

4. Three-dimensional neutrally buoyant displacements

The above analysis demonstrates that the dynamical evolution of two-dimensional heterogeneous displacements depends on the dominant wavelengths of the viscous and permeability vorticities, and on their relative magnitude compared to the length scale governing the corresponding homogeneous displacement. The ratios of these three length scales determine if the flow is dominated by viscous fingering, resonant amplification, or dispersion.

Our recent linear stability analysis of neutrally buoyant, *three-dimensional* homogeneous displacements in nominally axisymmetric geometries shows that they are governed by helical waves whose most unstable axial wavenumber component changes over time (Riaz & Meiburg 2003*a*). The subsequent nonlinear investigation of such homogeneous displacements (Riaz & Meiburg 2003*b*) indicates that this time dependence of the dominant vertical length scale leads to a large-scale redistribution of concentration gradients, which provides an extra source of instability to the system. How this interaction of vertical and horizontal modes affects the characteristics of three-dimensional heterogeneous displacements is the main issue to be addressed in the following.

4.1. *Periodic permeability variation*

Similarly to the two-dimensional case, we first analyse a periodic permeability variation constructed as

$$k(x, y, z) = \exp\{\gamma \cos(2\pi l x)\cos(2\pi m y)\cos(2\pi n z)\}, \tag{4.1}$$

where l, m, and n denote the wavenumbers in the x-, y- and z-directions, respectively. Below we typically employ $l = m$, but vary n independently. Figure 12 shows the $c = 0.5$ isosurfaces for a set of neutrally buoyant simulations with $Pe = 400$, $R = 2.5$, $G = 0$, and $s = 0.1$ for various values of m. In conjunction with a vertical wavenumber

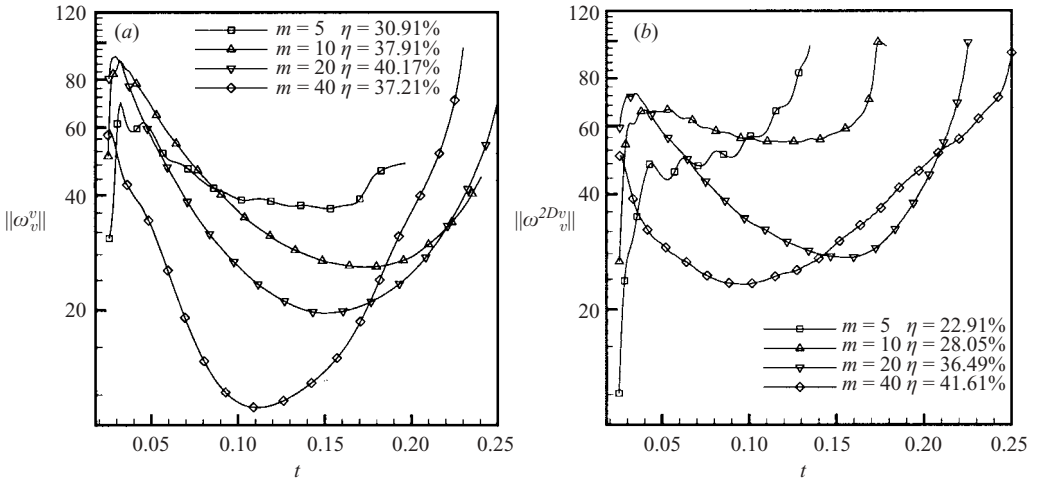

FIGURE 13. Comparison of the viscous vorticity norms for $Pe = 400$, $R = 2.5$, $s = 0.1$. (*a*) Three-dimensional case with $G = 0$ and $n = 12$. The norm $\|\omega_v^v\|$ is based upon the vertical component of the viscous vorticity. (*b*) $\|\omega_v^{2D}\|$ for the two-dimensional case. □, $m = 5$; △, $m = 10$; ▽, $m = 20$; ◇, $m = 40$. A higher level of instability for three-dimensional displacements at early times leads to $\|\omega_v^v\| > \|\omega_v^{2D}\|$. At later times, the interaction of horizontal and vertical modes for the three-dimensional case leads to $\|\omega_v^v\| < \|\omega_v^{2D}\|$, which results in an improvement of the breakthrough efficiency.

$n = 12$, the aspect ratio $A = 1/8$ results in 1.5 wavelengths in the vertical direction. Within horizontal planes the interfacial shapes are similar to their two-dimensional counterparts. Thus, in the $m = 5$ and 10 cases in figures 12(*a*) and 12(*b*) the fingers along the main diagonal evolve relatively freely, i.e. the displacement is dominated by viscous fingering. The $m = 20$ case in figure 12(*c*) shows a transition to the dispersive regime, in which dispersion reduces the finger amplitude. The dispersion-induced transition to a higher effective horizontal wavelength is observed for the $m = 40$ case in figure 12(*d*). In order to assess how the vertical permeability variations affect these displacements, we analyse again the vorticity norms.

Norms of the vertical viscous vorticity component shown in figure 13 reveal significant differences between the two- and three-dimensional displacements. Initially higher values of the vorticity norm for the three-dimensional case are consistent with our results of homogeneous displacements (Riaz & Meiburg 2003*b*), which show three-dimensional flows to be more unstable than their two-dimensional counterparts. However, note that for later times ($t > 0.05$), the vorticity norms decay more rapidly in three dimensions than in two. This reflects an overall damping effect in three-dimensional flows due to vertical permeability variations. Consequently, figure 13 indicates higher efficiencies for three-dimensional displacements than for the corresponding two-dimensional flows, for all m values except 40. For this large value of $m = 40$ notice that the norm decays rapidly and then rises steeply to achieve an efficiency lower than either the $m = 10$ or the $m = 20$ case. Inspection of figure 12(*d*) shows that the large-scale structures do not interact with each other and apparently cannot be affected by very small-scale permeability variations, hence they move more rapidly towards the production well compared to those shown in figures 12(*b*) and 12(*c*).

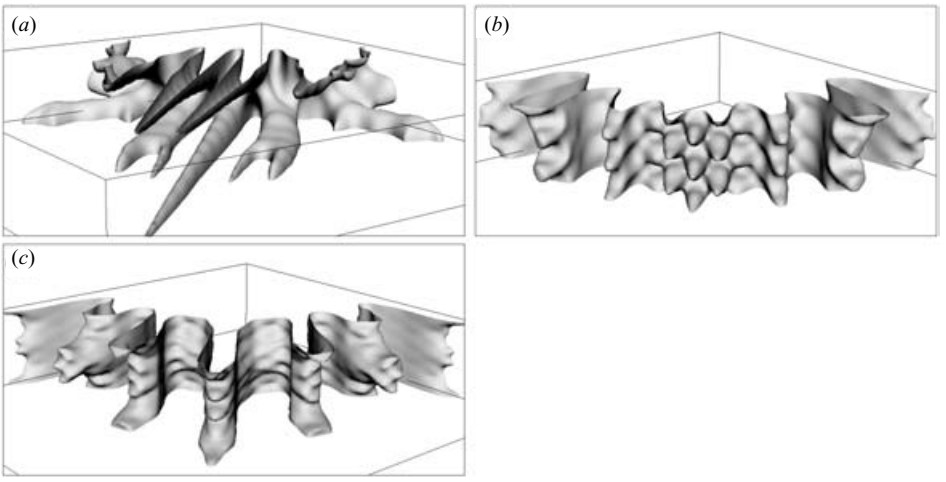

FIGURE 14. Concentration isosurfaces for $Pe = 400$, $R = 2.5$, $G = 0$, $A = 1/8$, $s = 0.1$, $m = 10$ and (*a*) $n = 4$, (*b*) $n = 20$, (*c*) $n = 40$. With an increase in n, fingers tend to interact, merge and form large-scale vertical structures as a result of the dispersive regime.

Figure 14 demonstrates the influence of the vertical permeability wavenumber in displacements with the same parameters as those in figure 12, for $m = 10$ and various values of n. For a small value of $n = 4$, the fingers in different horizontal planes do not interact strongly with each other, and breakthrough is quickly achieved (figure 14*a*). The case of $n = 12$ is shown in figure 12(*b*), which indicates some level of vertical finger interaction. At the higher value of $n = 20$ (figure 14*b*), a transition to dispersive behaviour can be observed. The interface tends to develop vertical structures on a scale significantly larger than the vertical permeability wavelength. Finally, the still higher value of $n = 40$ is dominated by dispersion (figure 14*c*), and a strong shielding effect in the horizontal planes arises due to the large vertical structures.

Figure 15 compares the breakthrough efficiencies for various values of n and m. The straight dotted lines show the corresponding data for the two- and three-dimensional homogeneous cases. As described in our earlier investigation (Riaz & Meiburg 2003*b*), the three-dimensional homogeneous case is more unstable, and has a lower efficiency, than its two-dimensional counterpart. The bold solid line represents the efficiency values for the two-dimensional heterogeneous case. For small values of the horizontal permeability wavenumber m, all but the lowest value of the vertical wavenumber n give rise to strong fingering interactions and dispersion, which stabilize the displacement and lead to higher efficiencies than for the two-dimensional heterogeneous case. On the other hand, for $n = 4$ the three-dimensional displacement is in the viscous fingering regime, and hence more unstable than the corresponding two-dimensional case. Note that the highest efficiencies are achieved for the intermediate vertical wavenumbers of $n = 12$ and 20. For $n = 40$ large-scale fingering structures are generated, which again has a destabilizing effect. The behaviour of η as a function of n can be attributed to similar effects, i.e. small n values are more unstable while intermediate values are the most stable due to dispersion and finger interaction. Higher n values are again unstable due to the generation of large-scale isolated structures as shown in figure 14(*c*) which do not interact and also cannot be effectively dispersed by very small correlation lengths. For some parameter combinations three-dimensional

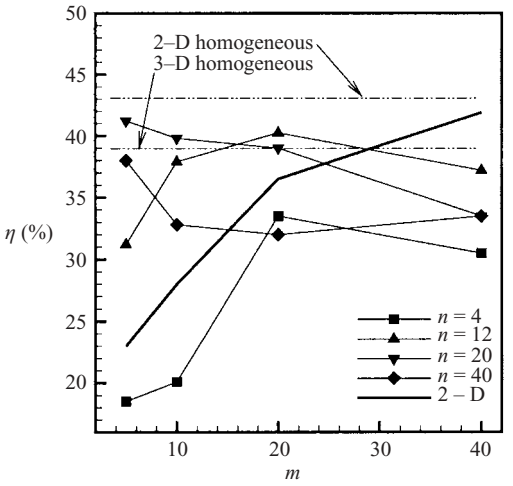

FIGURE 15. Comparison of the breakthrough efficiency η between two- and three-dimensional displacements for various values of n as function of m. $Pe = 400$, $R = 2.5$, $G = 0$, and $s = 0.1$. The absence of horizontal and vertical mode interactions results in a low efficiency for three-dimensional displacements at $n = 4$. Dispersion and finger interactions improve the efficiency for higher n and m values. For some parameter combinations, η for three-dimensional heterogeneous displacements can be larger than for three-dimensional homogeneous displacements.

heterogeneous displacements are stabilized to the extent that their efficiency is larger than that of the corresponding homogeneous flow, as shown in figure 15. In contrast, two-dimensional heterogeneous displacements always show a lower efficiency than the corresponding homogeneous case.

4.2. *Random permeability variation*

The three-dimensional random permeability field is constructed similarly to its two-dimensional counterpart given by equation (3.8). Figure 16 presents $c = 0.5$ isosurfaces for various values of m and n, with $Pe = 400$, $R = 2.5$, $G = 0$, $A = 1/8$ and $s = 0.1$ at $t = 0.04$. Figure 16(a) shows the cases of $m = 5$ at $n = 20$ to be dominated by the viscous fingering regime. The interaction among the fingers is seen to become more intense for $m = 40$ (figure 16c). Pairing and shielding interactions are already evident at the early time of $t = 0.04$, leading to the generation of large-scale structures that indicate the transition from the viscous fingering to the dispersive regime.

By keeping the horizontal wavenumber m constant and increasing the vertical permeability wavenumber n, we observe a similar transition from the viscous fingering regime shown in figure 16(b) to the dispersive regime shown in figure 16(d).

Figure 17 shows the ratio of the viscous and permeability vorticity vector norms. It indicates that the $m, n = 5, 10, 20$ displacements are dominated by the viscous fingering regime ($\|\omega_v\|/\|\omega_p\| > 1$) for early times. The $m = 40$ and $n = 40$ cases soon enter the dispersive regime due to the rapid increase in the viscous length scale. On the other hand, the cases $m = 5$ and 10 in figure 17(a), and $n = 5$ and 10 in figure 17(b) remain in the viscous fingering regime throughout the entire displacement. The $m = 20$ and $n = 20$ cases are on the border of the viscous fingering and the dispersive regimes.

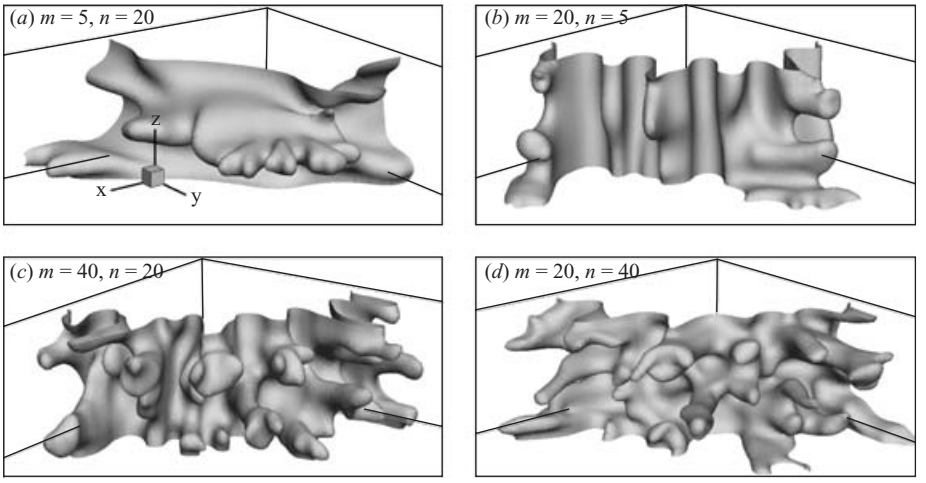

FIGURE 16. Concentration isosurfaces for three-dimensional displacements through random permeability distribution for $Pe = 400$, $R = 2.5$, $G = 0$, $A = 1/8$, $s = 0.1$ and various values of m and n at $t = 0.04$. An increase in either the horizontal or the vertical permeability wavenumber generates a more complex interfacial structure, increasing the possibility of fingering interactions. As a result the generation of structures much larger than the correlation length increases the possiblity of dispersive behaviour at later times, as shown in figure 17.

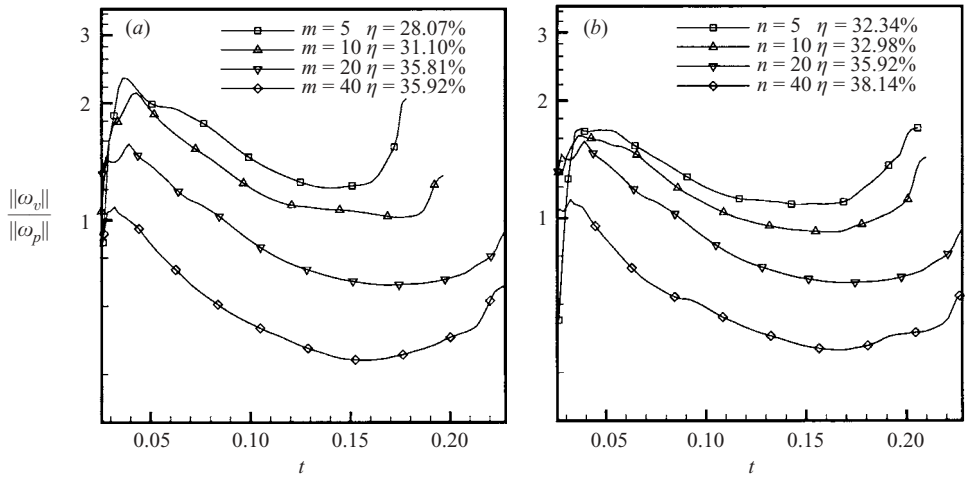

FIGURE 17. Ratio of the norms of the viscosity and permeability related vorticity for $Pe = 400$, $R = 2.5$, $G = 0$, $A = 1/8$, $s = 0.1$. (*a*) $n = 20$ various m values. (*b*) $m = 20$, various n values. For the smaller m and n values, the displacement is in the viscous fingering regime ($\|\omega_v\|/\|\omega_p\| > 1$) at early times. For later times, the $m = 20$ case transitions into the dispersive regime ($\|\omega_v\|/\|\omega_p\| < 1$).

5. Three-dimensional displacements with gravity override

The difference in density between injected and displaced fluid introduces an additional vorticity component. If the injected fluid is lighter than the displaced fluid, this gravitational vorticity can give rise to a gravity layer, which substantially alters the characteristics of the flow (Tchelepi & Orr 1994; Ruith & Meiburg 2000). Within the gravity layer the fingers are enhanced, while in the underride region they

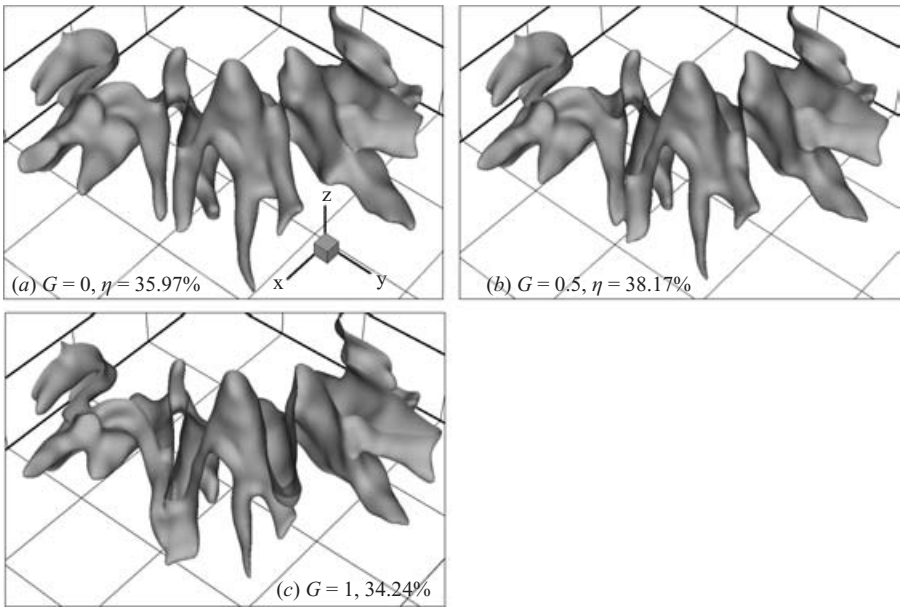

FIGURE 18. Concentration isosurfaces for the gravity override case. $Pe = 400$, $R = 2.5$, $s = 0.1$, $m = 20$, $n = 20$, $t = 0.14$ and various values of G. By encouraging the development of a gravity layer along the top boundary, the dominant fingers close to the lower boundary are weakened, resulting in an improvement in efficiency as G goes from $0 \rightarrow 0.5$. Further increase in the gravity override effect at $G = 1$ strengthens the fingers in the gravity layer resulting in a reduction in efficiency. Due to the coupling between viscous and permeability vorticities, the gravity override effect is weaker than in homogeneous displacements.

are suppressed. For homogeneous quarter five-spot displacements, a larger gravity parameter G generally results in earlier breakthrough, although for some parameter combinations intermediate values of G have been observed for which the efficiency is optimized due to specific interactions between the horizontal and vertical modes (Riaz & Meiburg 2003*b*). Two-dimensional rectilinear displacements (Camhi *et al.* 2000) demonstrate that the effect of gravity override is considerably reduced by permeability heterogeneities, due to the coupling between the viscous and permeability vorticities. As a result, an optimal efficiency is achieved at an intermediate variance level.

The influence of gravity override is shown in figure 18 for a representative combination of displacement parameters, at various values of the gravity parameter G. Comparison of the $G = 0.5$ case in figure 18(*b*) with the $G = 0$ case in figure 18(*a*) shows that gravity override strengthens the fingers close to the upper boundary, while weakening those near the lower boundary. While the gravity layer is not as pronounced for the present heterogeneous case as it is for the corresponding homogeneous case (Riaz & Meiburg 2003*b*), a slight diversion of the flow from the underride region to the gravity layer for $G = 0.5$ slows the rapid movement of the dominant fingers in the underride region observed for $G = 0$ in figure 18(*a*). Consequently, for the case $G = 0.5$ figure 18(*b*) shows that the gravity layer fingers are slightly stronger than the $G = 0$ case, which results in an improvement of the efficiency. It should be pointed out that the maximum in the recovery curve for an intermediate G in the above case is due to the location of the dominant flow path in the underride region. If the flow

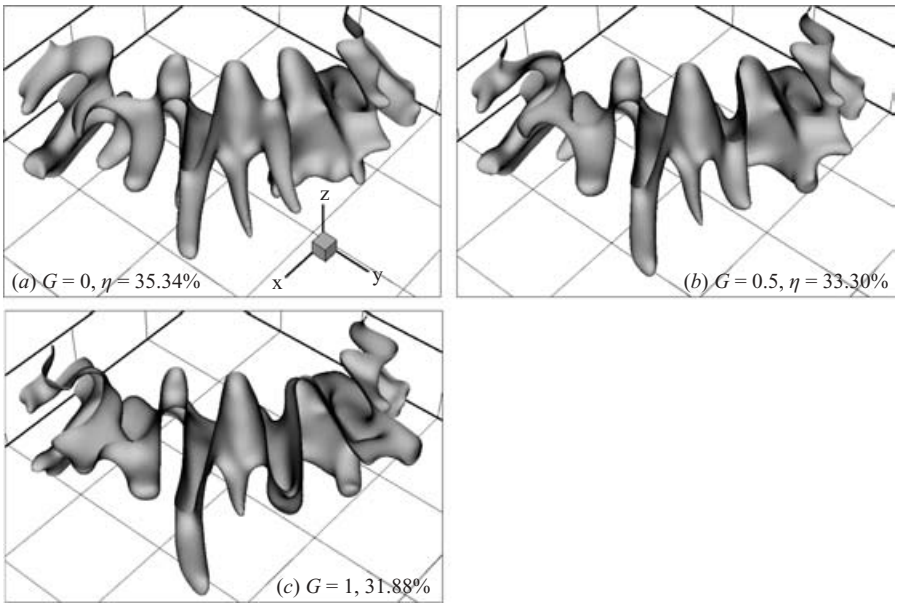

FIGURE 19. Concentration isosurfaces for the same cases as in figure 18, but with a lower variance $s = 0.01$. The lower level of heterogeneity allows the gravity layer to develop relatively freely, which results in a monotonic decrease in efficiency. The higher efficiency for the $s = 0.1$ case as compared to $s = 0.01$ for $G = 0$ is due to a weakening of the gravity layer, as well as the strengthening of the off-diagonal fingers, at $s = 0.1$.

path with the lowest resistance were instead located close to the upper boundary, there would be a monotonic decrease in efficiency with increasing G.

Note that the gravity layer is relatively weak for the present heterogeneous case, as compared to the corresponding homogeneous flow (Riaz & Meiburg 2003*b*). This fact, which is similar to observations for rectilinear flows, indicates that at the level of $s = 0.1$ the heterogeneity is already too strong for the coupling between the viscous and permeability vorticities to be effectively modified by the gravitational vorticity component. This is confirmed by figure 19, which depicts the same flows as figure 18, except that $s = 0.01$. Here the gravity layer is much stronger, which leads to a lower breakthrough efficiency for $s = 0.01$ than for $s = 0.1$, for both $G = 0.5$ and 1.

The above observation reflects the fact that the dominant path is selected not only on the basis of its permeability. Also important is its potential to support a resonant amplification, which partly depends on its geometric nature, and also on the local flow rate, which in turn is a function of the overall gravitational effect. Hence, the flow can select a relatively low-permeability path over one with higher permeability, as long as it supports a strong resonant amplification.

The relatively weak dependence of heterogeneous displacements on the gravity parameter, as compared to their homogeneous counterparts, is also reflected in the norms of the vertical and horizontal viscous vorticity fields. Since gravitational effects primarily result in horizontal vorticity, it is instructive to analyse the ratio of the vertical to the horizontal viscous vorticity norms $\|\omega_v^v\|/\|\omega_v^h\|$, shown in figure 20. We vary both the horizontal (m, figure 20*a*) and the vertical (n, figure 20*b*) permeability wavenumber. In each case the homogeneous displacement is more strongly affected by the horizontal vorticity, i.e. by gravitational effects, than any of the heterogeneous

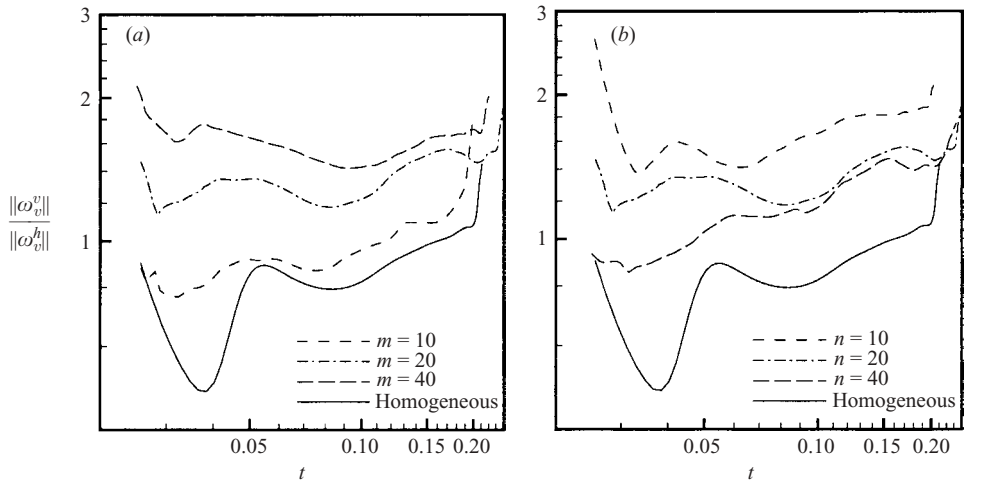

FIGURE 20. Ratio of the vertical and horizontal viscous vorticity norm. $Pe = 400$, $R = 2.5$, $G = 0.5$, $s = 0.1$, $A = 1/8$, (*a*) $n = 20$, (*b*) $m = 20$. Gravity override increases the relative strength of disturbances in the vertical direction, which are associated with horizontal vorticity. For the homogeneous case $\|\omega_v^v\|/\|\omega_v^h\| < 1$. On the other hand, the ratio exceeds unity for most heterogeneous cases, which implies that the perturbations in the horizontal directions are dominant. The ratio decreases with increasing m, while it increases with n.

displacements. Note that the influence of gravity, as measured by $\|\omega_v^v\|/\|\omega_v^h\|$, decreases with m, while it increases with n.

As seen above, individual random realizations of the permeability field can strongly influence the fingering dynamics, and consequently the displacement efficiency. We have not attempted to run sufficiently many simulations in order to obtain statistically significant averages, due to the prohibitive computational expense. Instead, we have limited ourselves to identifying the generic mechanisms which govern heterogeneous displacements. The accurate prediction of the displacement efficiency for a specific permeability field would, of course, require complete knowledge of the permeability distribution (Zhan & Yortsos 2001).

6. Summary and conclusions

The present investigation attempts to unravel the vorticity interaction mechanisms governing miscible displacements in heterogeneous porous media. Towards this end, we conduct three-dimensional simulations in the regimes of viscous fingering, dispersion (Waggoner *et al.* 1992; Tchelepi & Orr 1994; De Wit & Homsy 1997*b*; Camhi *et al.* 2000), and resonant amplification (De Wit & Homsy 1997*a*). The computational results are analysed in detail with respect to the characteristic wavenumbers and norms associated with the various components of the overall vorticity field. Only the combined information obtained from these diagnostic quantities allows us to identify and establish the mechanisms dominating specific flows. The nature of the displacement is discussed as a function of the relative magnitudes of the three length scales associated with the viscous vorticity, the permeability vorticity, and the corresponding homogeneous flow, respectively. Nominally axisymmetric displacements are particularly interesting in this respect, since some of the characteristic length scales grow in time as the front expands radially. This leads to displacement

flows that can undergo resonant amplification for a limited duration, while being dominated by fingering or dispersion at other times. Furthermore, the simulation results provide insight into how gravity affects the interactions among these length scales.

In a first step, the governing mechanisms are analysed for the conceptually simpler problem of spatially periodic permeability variations. We confirm that the resonant amplification is strongest when the permeability wavenumber is close to that of the corresponding homogeneous displacement. Random permeability distributions give rise to somewhat more complex displacements, due to the fact that they contain a range of length scales that have the potential to interact with the viscous instability. Comparisons among displacements for different parameter combinations highlight an important aspect regarding the selection of preferential flow paths: The displacement does not necessarily proceed most rapidly along maximum permeability channels. Rather, the selection is governed by both the local permeability values and the potential for resonant amplification along a given path. Therefore, the overall displacement parameters such as the Péclet number, the viscosity ratio or the gravity parameter all influence the effective path resistance.

Overall, three-dimensional neutrally buoyant displacements are seen to be qualitatively similar to their two-dimensional counterparts. However, for late times the interaction of the horizontal and vertical modes in three dimensions leads to a more subdued growth as compared to two-dimensional displacements, which results in a higher breakthrough efficiency. In the presence of density differences, the potential for gravity override becomes important. While this effect is seen to play a dominant role in homogeneous displacements, it is suppressed to some extent in heterogeneous displacements, even for relatively small values of the heterogeneity variance. This is a result of the coupling between the viscous and permeability vorticity fields, particularly for the viscous fingering and resonant amplification regimes. In the dispersive regime, gravity override is somewhat more effective because the coupling between the viscous and permeability vorticity fields is less pronounced, so that the large-scale structures become more responsive to buoyancy effects. This is confirmed by the ratio of the vertical to the horizontal viscous vorticity norm, which decreases with increasing values of the vertical correlation wavenumber.

In the present investigation, we were able to touch upon the effects of different random realizations of the heterogeneity field only briefly. This issue will have to be addressed in more detail in order to obtain relevant statistical information regarding such global quantities as the breakthrough efficiency.

The authors thank Professor G. M. Homsy and Professor Hamdi Tchelepi for several helpful discussions. Support for this research by the Department of Energy, Office of Basic Energy Sciences, the Chevron Petroleum Technology Company, the Petroleum Research Fund, as well as through an NSF equipment grant is gratefully acknowledged.

REFERENCES

Araktingi, U. G. & Orr, F. M. J. 1988 Viscous fingering in heterogeneous porous media. *SPE Paper* 18095.

Camhi, E., Ruith, M. & Meiburg, E. 2000 Miscible rectilinear displacements with gravity override. Part 2. Heterogeneous porous media. *J. Fluid Mech.* **420**, 259.

Canuto, C., Hussaini, M. Y., Quarteroni, A. & Zang, T. A. 1986 *Spectral Methods in Fluid Dynamics*. Springer.

Chen, C.-Y. & Meiburg, E. 1998*a* Miscible porous media displacements in the quarter five-spot configuration. Part 1. The homogeneous case. *J. Fluid Mech.* **371**, 233.

Chen, C.-Y. & Meiburg, E. 1998*b* Miscible porous media displacements in the quarter five-spot configuration. Part 2. Effect of heterogeneities. *J. Fluid Mech.* **371**, 269.

Christie, M. A. & Bond, D. J. 1987 Detailed simulation of unstable processes in miscible flooding. *SPE Res. Engng* p. 514.

De Wit, A. & Homsy, G. M. 1997*a* Viscous fingering in periodically heterogeneous porous media. I. Formulation and linear stability. *J. Chem. Phys.* **107, 22**, 9609.

De Wit, A. & Homsy, G. M. 1997*b* Viscous fingering in periodically heterogeneous porous media. II. Numerical simulations. *J. Chem. Phys.* **107, 22**, 9619.

Fletcher, C. A. J. 1991 *Computational Techniques for Fluid Dynamics*, 2nd edn. Springer.

Gottlieb, D. & Orszag, S. A. 1977 *Numerical Analysis of Spectral Methods: Theory and Applications.* Society for Industrial and Applied and Mathematics.

Kempers, L. J. T. M. & Haas, H. 1994 The dispersion zone between fluids with different density and viscosity in a heterogeneous media porous media. *J. Fluid Mech.* **267**, 299.

Lele, S. K. 1992 Compact finite differences with spectral-like resolution. *J. Comput. Phys.* **103**, 16.

Moissis, D. E., Miller, C. & Wheeler, M. F. 1989 Simulation of miscible viscous fingering using a modified method of characteristics: Effect of gravity and heterogeneity. *SPE Paper* 18440, p. 431.

Riaz, A. 2003 Three-dimensional miscible, porous media displacements in the quarter five-spot geometry. PhD thesis, Department of Mechanical and Environmental Engineering. University of California, Santa Barbara.

Riaz, A. & Meiburg, E. 2003*a* Radial source flows in porous media: Linear stability analysis of axial and helical perturbations in miscible displacements. *Phys. Fluids* **15**, 938.

Riaz, A. & Meiburg, E. 2003*b* Three-dimensional miscible displacement simulations in homogeneous porous media with gravity override. *J. Fluid Mech.* **494**, 95–117.

Ruith, M. & Meiburg, E. 2000 Miscible rectilinear displacements with gravity override. Part 1. Homogeneous porous medium. *J. Fluid Mech.* **420**, 225.

Shinozuka, M. & Jen, C. M. 1972 Digital simulations of random processes and its application. *J. Sound Vib.* **25**, 111.

Sorbie, K., Farag Feghi, Pickup, G. E., Ringrose, G. E. & Jenson, J. L. 1992 Flow regimes in miscible displacements in heterogeneous correlated random fields. *SPE/DOE Paper* 24140, p. 371.

Tan, C. T. & Homsy, G. M. 1987 Stability of miscible displacements in porous media: Radial source flow. *Phys. Fluids* **30**, 1239.

Tan, C. T. & Homsy, G. M. 1992 Viscous fingering with permeability heterogeneity. *Phys. Fluids* A **4**, 1099.

Tchelepi, H. A. 1994 Viscous fingering, gravity segregation and permeability heterogeneity in two dimensional and three dimensional flows. PhD thesis, Department of Petroleum Engineering, School of Earth Sciences, Stanford University.

Tchelepi, H. A. & Orr, F. M. J. 1993 Dispersion, permeability heterogeneity and viscous fingering: Acoustic experimental observations and particle tracking simulations. *Phys. Fluids* **5**, 1558.

Tchelepi, H. A. & Orr, F. M. J. 1994 Interaction of viscous fingering, permeability inhomogeneity and gravity segregation in three dimensions. *SPE Res. Engng*, p. 266.

Waggoner, J. R., Castillo, J. L. & Lake, L. L. 1992 Simulation of EOR processes in stochastically generated permeable media. *SPE Form. Eval.* p. 173.

Zhan, L. & Yortsos, Y. C. 2001 A direct method for the identification of the permeability field of an anisotropic porous medium. *Water Resour. Res.* **37**, 1929.

Zhang, H. R., Sorbie, K. S. & Tsibuklis, N. B. 1997 Viscous fingering in five-spot experimental porous media: New experimental results and numerical simulations. *Chem. Engng Sci.* **52**, 37.